Wavelet multiresolution analysis of particle-laden turbulence

Maxime Bassenne,[*] Parviz Moin, and Javier Urzay

Center for Turbulence Research, Stanford University, Stanford, California 94305-3024, USA

Direct numerical simulations of incompressible homogeneous-isotropic turbulence laden with a dilute suspension of inertial point particles are performed in conjunction with a wavelet multiresolution analysis of the results. The use of spatially localized wavelet basis functions enables the simultaneous consideration of physical and scale spaces in the spectral characterization of the flow field of the carrier phase and the concentration field of the dispersed phase. The multiresolution analysis of the dispersed phase provides statistical information about the spatial variabilities of a scale-dependent coarse-grained number density field and the local energy spectra of its fluctuations, characterizing the sensitivities of those quantities to variations in scale and Stokes number. In particular, the spatial variabilities of the wavelet energy spectrum of the particle concentration fluctuations are observed to be maximum in regimes where the particles preferentially concentrate. The results highlight the scale-dependent inhomogeneities of the structures in the concentration field generated by preferential concentration, and the existence of characteristic scales of interaction between the dispersed and carrier phases. Additionally, an interphase multiresolution analysis is performed that indicates the occurrence of a spatial anticorrelation between the enstrophy and kinetic-energy spectra of the carrier phase and the particle concentration at small scales in regimes where preferential concentration is important. This anticorrelation vanishes as the scale is increased and is largely suppressed when the preferential-concentration effect is negligible.

I. INTRODUCTION

The wealth of flow structures and spatiotemporal scales present in high-Reynolds-number flows have important consequences for the motion of suspended inertial particles. One relevant effect is preferential concentration, whereby the particles tend to accumulate in clouds. The preferential concentration of inertial particles is an important physical phenomenon in multiphase turbulent flows of practical relevance [1–7]. In addition, the spatial inhomogeneities arising in the concentration of particles as a result of the preferential-concentration effect are central to the relative dispersion and interphase coupling with the turbulent environment [8–14].

The study of preferential concentration from a theoretical perspective is limited by the inherent complexity of turbulent flows. Robinson [15] was the first to establish an analytical framework for the accumulation of particles by noticing that the dispersed phase is compressible and that in strained, irrotational incompressible flows the number density of particles increases monotonically in the Lagrangian frame. These results have been employed in subsequent studies to improve the understanding of aerodynamic focusing of aerosols [16] and the dispersion and vaporization of fuel sprays [17,18].

---

[*]Corresponding author: bassenne@stanford.edu

The occurrence of preferential concentration of small particles in homogeneous-isotropic turbulent flows largely depends on the Stokes number

$$\mathrm{St}_k = t_a/t_k, \tag{1}$$

where t_a is the characteristic particle acceleration time and t_k is the Kolmogorov timescale, which can be related to the integral-scale turnover time t_ℓ through the Reynolds number $\mathrm{Re}_\ell = (t_\ell/t_k)^2 \gg 1$. For instance, for large St_k such that $\mathrm{St}_k/\mathrm{Re}_\ell^{1/2} \gg 1$, the particles move ballistically with respect to turbulent eddies and their trajectories are largely independent of the turbulence dynamics. Conversely, for $\mathrm{St}_k \ll 1$, the particles become flow tracers and sample unbiasedly all flow structures during their flight time. At intermediate values, $\mathrm{St}_k \sim 1$, a relevant regime emerges in which the particles preferentially concentrate in small-scale clouds in homogeneous-isotropic turbulent flows [19,20]. In this regime, the particles trace the large and midsized eddies but slip on the small ones, thereby leading to interphase relative motion with characteristic velocity of the same order as the fluctuating velocity of the Kolmogorov eddies, $u_k \sim \ell_k/t_k$, where $\ell_k = (\nu t_k)^{1/2}$ is the Kolmogorov length. This effect maximizes the variance of the particle number-density field and produces a high-wavenumber peak in the spectral energy of the concentration fluctuations [21,22].

The phenomenon of preferential concentration in homogeneous-isotropic turbulence at $\mathrm{St}_k \sim 1$ is caused by the high levels of internal intermittency in the small scales of turbulence, which are known to simultaneously bear the largest vorticity and strain rates, both distributed unevenly in spotty regions in space [23]. Specifically, the particles, which display finite inertia with respect to the small eddies, are centrifuged from the intense small vortices and concentrate preferentially in interstitial zones where the strain rate is large, leading to high-wavenumber structures of particle concentration. In inhomogeneous flows where large coherent structures develop, such as particle-laden turbulent jets or mixing layers, preferential concentration of particles may also occur at large scales through a mechanism unrelated to intermittency, when the particle acceleration time becomes of the same order as the integral time, i.e., $\mathrm{St}_k/\mathrm{Re}_\ell^{1/2} \sim 1$. In those flows, the particles are clearly observed to accumulate along large-scale saddle zones perpendicular to the braids in between coherent vortical structures, giving rise to elongated particle clouds [1,24].

A number of computational investigations of preferential concentration have been performed either in physical or Fourier spaces [8,20,21,25]. In contrast, the present work deploys wavelet basis functions for the analysis. Wavelet methods have been used in the past to study the structure of turbulent flows [26–31]. The particular choice of wavelets made here is best motivated by two different aspects related to preferential concentration, which are illustrated by the particle concentration fields shown in the simulation results in the first three rows of Fig. 1 corresponding to three different Stokes numbers $\mathrm{St}_k = 0.1$, 1, and 10 (details of the computational setup are provided later in the text in Sec. II).

The first aspect to note in Fig. 1 is the presence of small-scale, sparse filamentous structures in the spatial distribution of particles, which are most discernible in the second row of Fig. 1 corresponding to the case $\mathrm{St}_k = 1$. The spatial localization of these structures makes them not ideally suited for Fourier spectral analyses, which inevitably entail spatial delocalization of the transformed quantities because of the infinite spatial support of the Fourier basis functions. On the other hand, the finite spatial support of the wavelet basis functions enables the examination of the spatially localized spectral characteristics of the concentration field.

The second aspect to note in Fig. 1 is related to the multiscale nature of preferential concentration in the following sense. At large scales, corresponding to the left column of Fig. 1, the visualization of the spatial distribution of particles at the three Stokes numbers treated here appear to contain clouds where particles accumulate. This is clearly evidenced by comparing the first three panels in the first column of Fig. 1 with the bottom one in the same column, which corresponds to a spatial distribution of particles obtained from randomly dispersing approximately the same number of particles in the computational domain. However, upon examining increasingly smaller scales, which are represented by the enlarged panels in the second, third, and fourth columns in Fig. 1, the
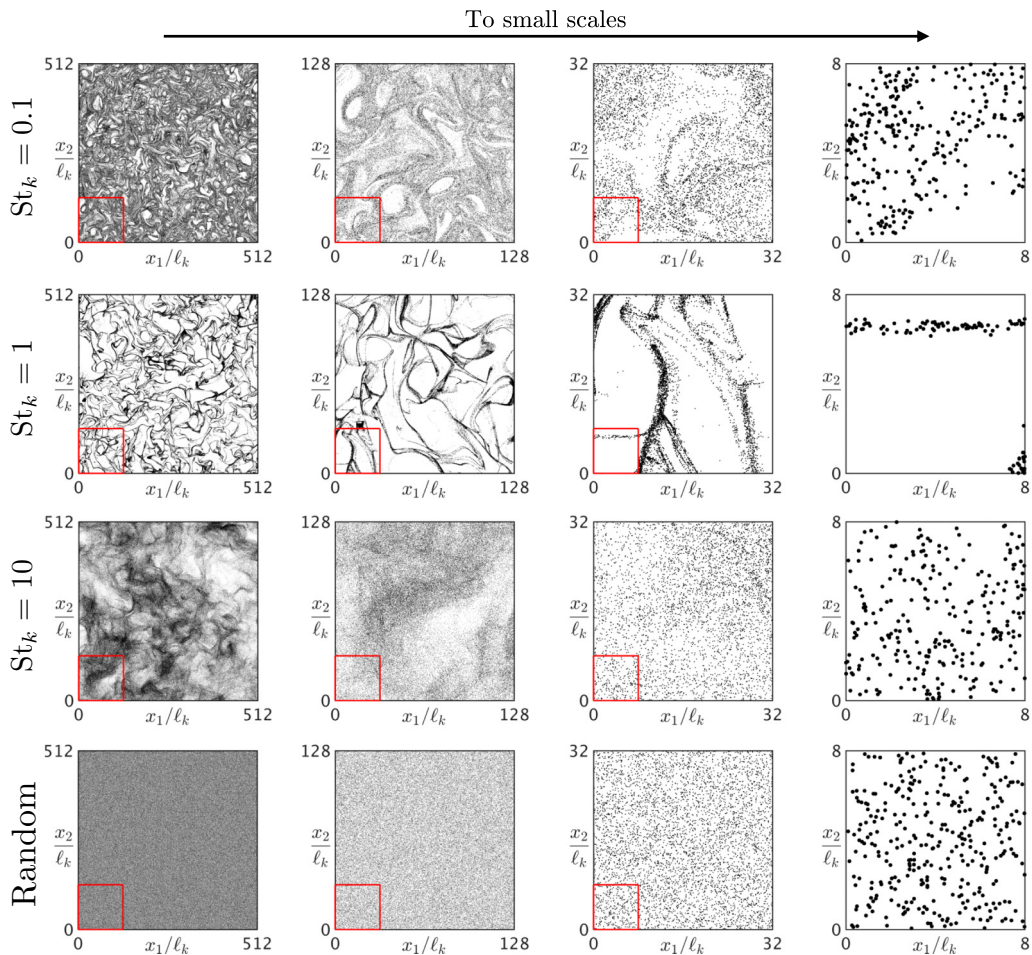
FIG. 1. Spatial distribution of particles (black dots) in a two-dimensional cross section of thickness equal to one Kolmogorov length for three different Stokes numbers: $St_k = 0.1$ (first row), $St_k = 1$ (second row), and $St_k = 10$ (third row) obtained from DNS of particle-laden homogeneous-isotropic turbulence (see Sec. II for further details on the computational setup). The fourth row corresponds to randomly distributed particles with the same total number of particles as above. Second to fourth columns are $\times 4$ magnified view of the solid-red-line contoured subregion in the nearest left column. The first column represents a full-scale cross section of the entire computational domain.

qualitative conclusions that can be drawn change significantly with respect to the aforementioned visualization at the large scales. For instance, the cases $St_k = 0.1$ and $St_k = 10$ display increasingly less preferential concentration of particles as the figures are enlarged, leading to dispersed particle fields at the small scales (i.e., see first and third panels in the last column of Fig. 1). In contrast, the filamentous patterns observed at the large scales persist all the way down to the Kolmogorov scale in the case $St_k = 1$. Given this dependency of the observations on the spatial scales, it is of some interest to use wavelet basis functions in order to study scale-dependent metrics of preferential concentration associated with particular regions of the flow field.

   In this study, a discrete wavelet multiresolution analysis is employed for investigating interphase conditioned spectral statistics in particle-laden homogeneous-isotropic turbulence. The results include wavelet-based localized spectra of kinetic energy, enstrophy, and particle concentration energy, along with the corresponding spatial fluctuations that enable the quantification of

scale-dependent probability density functions (PDFs) and spatially cross-correlated spectral dynamics between carrier and dispersed phases.

The outline of this paper is as follows. The computational setup is described in Sec. II. Section III is devoted to describing the results of the wavelet analysis for each separate phase along with the analysis of interphase conditioned statistics. Lastly, concluding remarks are given in Sec. IV.

II. COMPUTATIONAL SETUP

The computational setup employed in this study is the same as the one in Ref. [32], and therefore the details will be omitted here. In summary, the numerical code integrates the incompressible linearly forced Navier-Stokes equations in a triply periodic cubic domain with $N^3 = 512^3$ grid points. A total of $N_p = 670$ million monodisperse particles are tracked using a Lagrangian approach that integrates the equation of the trajectories along with a supplementary equation of motion for each particle that incorporates the Stokes drag. The mass-loading ratio is sufficiently small such that the influences of the particles on the gas are negligible. The turbulence is linearly forced according to the constant-dissipation method outlined in Ref. [33]. The numerical method consists of an energy-conserving finite-difference formulation with central second-order spatial discretizations and fourth-order Runge-Kutta time integration [34].

The resulting flow is a homogeneous isotropic turbulent one at a Taylor-Reynolds number $\mathrm{Re}_\lambda = (15 \mathrm{Re}_\ell)^{1/2} = 81$. The spatial resolution of the simulations is $\kappa_{\max} \ell_k = \pi$, where $\kappa_{\max} = \pi / \Delta$ is the largest wavenumber and Δ is the grid spacing. The ensemble-averaged Fourier spectra for kinetic energy $k = \langle u_i u_i \rangle / 2$ and enstrophy $\Omega = \langle \omega_i \omega_i \rangle$, denoted, respectively, by E_k and E_Ω, are shown in Figs. 2(a) and 2(b). In this formulation, u_i and ω_i are the fluid velocity and vorticity components, respectively. Similarly, for a general continuous field $y(\boldsymbol{x})$, the bracket operator $\langle y \rangle = 1/(N\Delta)^3 \int y(\boldsymbol{x}) d\boldsymbol{x}$ denotes the volumetric average.

The wavelet analysis shown below for the dispersed phase requires the estimation of an Eulerian number-density field $n(\boldsymbol{x})$ from the discrete Lagrangian particles. In this study, n is estimated by simply projecting the Lagrangian particles onto the nearest-neighbor point of the same grid used to solve the carrier-phase hydrodynamics. A snapshot of a resulting number-density field is shown in Fig. 2(c) for $\mathrm{St}_k = 1$, which has a strong visual resemblance to the corresponding discrete particle distributions provided in the panels of the second row in Fig. 1. The number of particles N_p is chosen such that the mean number-density is $\langle n \rangle = N_p/(N\Delta)^3 = 5/\Delta^3$.

Figure 2(d) shows the Fourier energy spectra of the number-density fluctuations $E_\mathcal{N}$ obtained from an artificially imposed, random spatial distribution of particles that follows a Poisson probability distribution function (PDF) with mean and variance equal to $\langle n \rangle$ and from distributions of particles computed using the present computational setup. These Fourier spectra can be interpreted as a decomposition of the total particle number-density field variance into single wavenumber contributions and will be analyzed further below. Note that the Fourier energy spectra of the number-density fluctuations increasingly resemble those of a random distribution at high wavenumbers when the Stokes number departs from unity. This effect has two different causes, namely, the finite number of particles used in the simulations, which engenders low-energy high-wavenumber noise, and the fact that the high-wavenumber range of $E_\mathcal{N}$ contains much less hydrodynamically induced energy for $\mathrm{St}_k = 0.1$ and $\mathrm{St}_k = 10$ than for $\mathrm{St}_k = 1$ because of the absence of preferential concentration in the two former cases, as illustrated in Fig. 2(d). Further analyses of the numerical noise resulting from finite values of N_p can be found in Ref. [32].

III. WAVELET MULTIRESOLUTION ANALYSIS

In this section, numerical results pertaining to the wavelet-based analysis of the carrier and dispersed phase flow fields are described. A summary of the wavelet mathematical relations involved in the analysis is also provided below for completeness. The reader is referred to the classic references [26,29,31,35,36] for further details about the formulation.
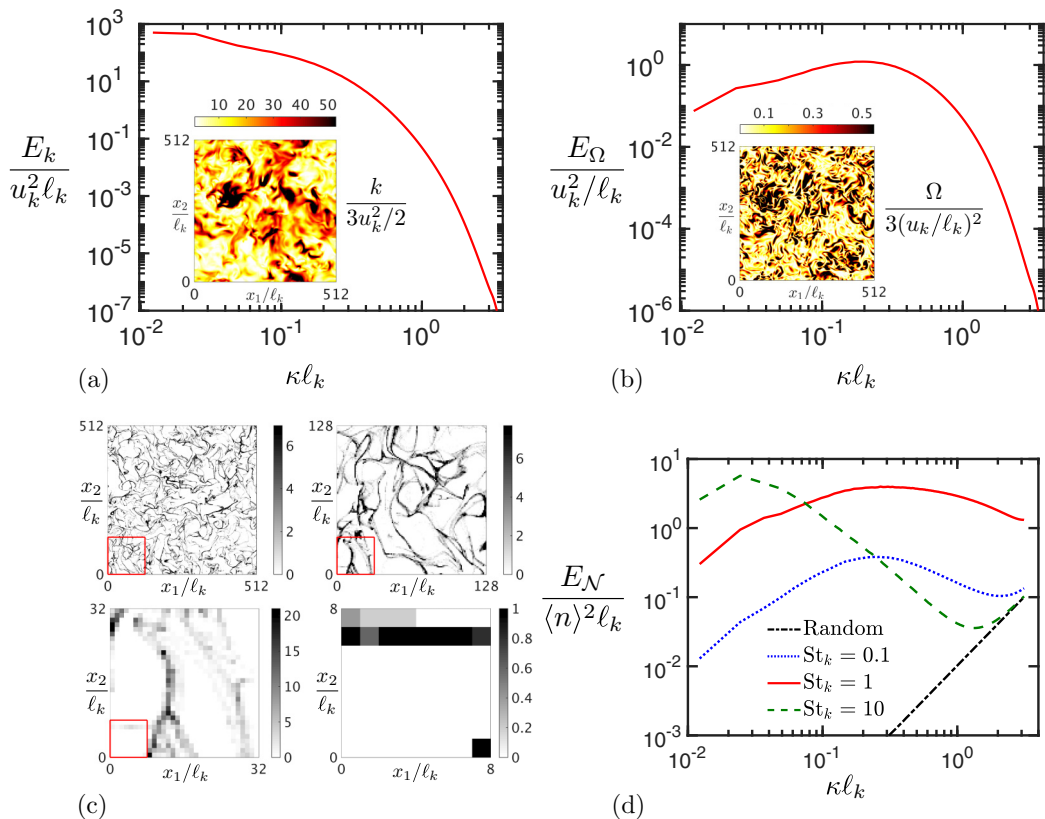
FIG. 2. Ensemble-averaged Fourier spectra for (a) turbulent kinetic energy and (b) enstrophy as a function of the wavenumber κ. Insets represent instantaneous midplane cross sections of the contours of (a) turbulent kinetic energy and (b) vorticity magnitude. In panel (c), instantaneous midplane cross sections of the particle number density are shown at different length scales for $St_k = 1$. Panel (d) shows the Fourier energy spectra of the particle number-density fluctuations for $St_k = 0.1$, 1, and 10 obtained with $\langle n \rangle = 5/\Delta^3$. Also included is the Fourier energy spectrum of the number-density fluctuations obtained from an artificially imposed, random spatial distribution of particles.

A. Wavelet formulation

Consider a three-dimensional (3D) scalar field y (for instance, the number density field n) discretely described in physical space by its pointwise values $y[\boldsymbol{x_0}]$ at cell-center locations

$$\boldsymbol{x_0} = 2^{-1}(i\Delta, j\Delta, k\Delta) \tag{2}$$

of the primitive computational grid employed in the numerical simulations described above, where $(i, j, k) = 1, 3, \ldots, 2N - 1$. A continuous wavelet-based representation of y is obtained as

$$y(\boldsymbol{x}) = \sum_{\boldsymbol{x_0}} \hat{y}^{(0)}[\boldsymbol{x_0}]\phi^{(0)}(\boldsymbol{x} - \boldsymbol{x_0}), \tag{3}$$

where the continuous physical space coordinate is denoted by $\boldsymbol{x}$. In Eq. (3), $\phi^0(\boldsymbol{x} - \boldsymbol{x_0})$ are scaling functions that form an orthonormal basis of low-pass filters centered at the wavelet collocation grid points $\boldsymbol{x_0}$, with the filter width being equal to the grid spacing Δ. The scaling functions are chosen to have unit energy $\langle \phi^0(\boldsymbol{x} - \boldsymbol{x_0})\phi^0(\boldsymbol{x} - \boldsymbol{x_0})\rangle = 1$ instead of unit integral $\langle \phi^0(\boldsymbol{x} - \boldsymbol{x_0})\rangle = 1$. Using

this constraint, the approximation coefficients

$$\hat{y}^{(0)}[\boldsymbol{x_0}] = \langle y(\boldsymbol{x})\phi^{(0)}(\boldsymbol{x} - \boldsymbol{x_0}) \rangle \tag{4}$$

can be derived from Eq. (3). In practice, when employing the numerical simulation data described above, Eq. (4) cannot be computed exactly, since y is only known at discrete points $\boldsymbol{x_0}$. Instead, it is numerically discretized and the approximation coefficients $\hat{y}^{(0)}[\boldsymbol{x_0}]$ are estimated as an algebraic function of $y[\boldsymbol{x_0}]$. Assuming that $\phi^0(\boldsymbol{x} - \boldsymbol{x_0})$ decays quickly away from $\boldsymbol{x} = \boldsymbol{x_0}$, the simplest estimate of Eq. (4) yields [26,35,37]

$$\hat{y}^{(0)}[\boldsymbol{x_0}] = y[\boldsymbol{x_0}]/N^{3/2}. \tag{5}$$

Equation (5) is the initialization stage of the recursive wavelet multiresolution algorithm (MRA) of Mallat [36], which enables the computation of wavelet coefficients.

The decomposition of the finest-scale low-pass filter $\phi^0(\boldsymbol{x} - \boldsymbol{x_0})$ in terms of narrow-band wavelet filters $\psi^{(s,d)}(\boldsymbol{x} - \boldsymbol{x_s})$ with increasingly large filter width and a coarsest-scale scaling function $\phi^{(S)}(\boldsymbol{x} - \boldsymbol{x_S})$ yields the full wavelet-series expansion of y (the reader is referred to Ref. [36] for more details)

$$y(\boldsymbol{x}) = \sum_{s=1}^{S} \sum_{\boldsymbol{x_s}} \sum_{d=1}^{7} \check{y}^{(s,d)}[\boldsymbol{x_s}]\psi^{(s,d)}(\boldsymbol{x} - \boldsymbol{x_s}) + \hat{y}^{(S)}[\boldsymbol{x_S}]\phi^{(S)}(\boldsymbol{x} - \boldsymbol{x_S}), \tag{6}$$

where

$$\check{y}^{(s,d)}[\boldsymbol{x_s}] = \langle y(\boldsymbol{x})\psi^{(s,d)}(\boldsymbol{x} - \boldsymbol{x_s}) \rangle \tag{7}$$

and

$$\hat{y}^{(S)}[\boldsymbol{x_S}] = \langle y(\boldsymbol{x})\phi^{(S)}(\boldsymbol{x} - \boldsymbol{x_S}) \rangle \tag{8}$$

are wavelet and approximation coefficients at scale s and S, respectively, obtained from the orthonormality properties of the wavelet and scaling functions $\psi^{(s,d)}(\boldsymbol{x} - \boldsymbol{x_s})$ and $\phi^{(S)}(\boldsymbol{x} - \boldsymbol{x_S})$. In this formulation, $d = (1, \ldots, 7)$ is a wavelet directionality index, and $s = (1, 2 \ldots, S)$ are scale exponents, with $S = \log_2 N = 9$ the number of resolution levels allowed by the grid. Similarly, $\boldsymbol{x_s} = 2^{s-1}(i\Delta, j\Delta, k\Delta)$ is a scale-dependent wavelet grid of $(N/2)^{3s}$ elements where the basis functions are centered, with $i, j, k = 1, 3, 5, \ldots, N/2^{s-1} - 1$. The wavelet coefficients $\check{y}^{(s,d)}[\boldsymbol{x_s}]$ represent the local fluctuations of y centered at $\boldsymbol{x_s}$ at scale s, while the approximation coefficient $\hat{y}^{(S)}[\boldsymbol{x_S}]$ is proportional to the volumetric mean of y. The wavelet and approximation coefficients (7) and (8) are computed using the MRA [36], with periodic boundary conditions being assumed for the field y.

At each scale, the filter width of the wavelets is given by the length scale

$$\ell_s = 2^s \Delta, \tag{9}$$

with $\ell_1 = 2\Delta = 2\ell_k$ and $\ell_9 = L = 512\ell_k$ corresponding to the smallest and largest length scales, respectively, where L is the side length of the computational domain. The length scale ℓ_s can be associated with the representative wavenumber

$$\kappa = 2\pi/\ell_s = 2\pi 2^{-s}/\Delta. \tag{10}$$

Using expression (10), the wavenumber κ, and the scale exponent s can be interchanged in the notation below.

In this study, the 3D orthonormal basis functions $\psi^{(s,d)}(\boldsymbol{x} - \boldsymbol{x_s})$ are taken to be products of one-dimensional (1D) Haar wavelets, as described in Ref. [26]. It should be noted that Haar wavelets have a narrow spatial support that provides a high degree of spatial localization, which is beneficial for capturing the small-scale zones where particles preferentially concentrate. However, Haar wavelets display large spectral leakage at high wavenumbers since infinite spectral and spatial resolutions cannot be simultaneously attained due to limitations imposed by the uncertainty principle [35].

Computations were performed using different wavelets, particularly those of wider spatial support such as Coifman wavelets with four vanishing moments, but less interesting dynamics were discerned when analyzing spatially cross-correlated spectral statistics between the carrier and dispersed phases. This is due to the fact that wavelets with wider spatial support do not have sufficient spatial resolution to capture the narrow, slender particle clouds present in preferentially concentrated flow regimes.

The definition of 3D wavelets as multiplicative products of 1D wavelets is a particular choice that follows the multiresolution analysis formulation described by Mallat [36]. In this framework, the multivariate wavelets are characterized by an isotropic scale and therefore render limited information about anisotropy in the flow [36]. A large number of alternative basis functions have been recently proposed for replacing traditional wavelets when analyzing multidimensional data that exhibit complex anisotropic structures such as filaments and sheets. These include, but are not limited to, curvelets, contourlets, and shearlets (see Ref. [38] for an extensive review on this topic). Application of these advanced multiscale geometric analysis tools to studying particle preferential concentration certainly warrant further investigation.

B. Carrier-phase wavelet-based statistics

In this wavelet framework, the local energy spectrum of y evaluated at $\boldsymbol{x}_s$ is defined as

$$\check{E}[\kappa, \boldsymbol{x}_s] = N^3 \frac{2^{-3s} r}{\delta \kappa} \sum_{d=1}^{7} \check{y}^{(s,d)}[\boldsymbol{x}_s] \check{y}^{(s,d)}[\boldsymbol{x}_s], \tag{11}$$

where κ is given by (10) and r is a prefactor that takes the values $r = 1/2$ for velocity and $r = 1$ for vorticity and scalars. The spatial average of the energy spectrum is given by

$$\check{E}(\kappa) = \langle \check{E}[\kappa, \boldsymbol{x}_s] \rangle_{\boldsymbol{x}_s}. \tag{12}$$

The definition (12) satisfies the energy constraint $\sum_{s=1}^{S} \check{E}(\kappa) \delta \kappa = r \langle y'(\boldsymbol{x})^2 \rangle$, where $y'(\boldsymbol{x}) = y(\boldsymbol{x}) - \langle y(\boldsymbol{x}) \rangle$ is the fluctuation and $\delta \kappa = 2\pi 2^{-s} \Delta^{-1} \ln 2$ [26].

Following these definitions, Figs. 3(a) and 3(b) shows the ensemble-averaged wavelet spectra $\check{E}_k$ and $\check{E}_\Omega$ for kinetic energy and enstrophy, respectively. At small wavenumbers, the mean wavelet spectrum resembles that of Fourier [see Figs. 2(a) and 2(b)], but differences emerge at high wavenumbers where spectral leakage occurs due to the narrow special support of the Haar wavelets, as noted in previous studies [39]. The results shown in Figs. 3(a) and 3(b) indicate that the spatial variabilities of the spectra are most pronounced at high wavenumbers, where most wavelet coefficients are small except for a few that correspond to relatively energetic structures, setting the mean value far above the mode of the distribution. The scale-conditioned PDFs of the spectra are similar to log-normal distributions, as observed in Figs. 3(c) and 3(d).

The velocity and vorticity fields become intermittent at the small scales, as shown in Figs. 3(a) and 3(b) by the scale-conditioned flatness factors of the wavelet coefficients of velocity $F_{\check{u}}(\kappa) = \langle \check{u}_1^{(s)4} \rangle_{\boldsymbol{x}_s} / \langle \check{u}_1^{(s)2} \rangle_{\boldsymbol{x}_s}^2$ and vorticity $F_{\check{\omega}}(\kappa) = \langle \check{\omega}_1^{(s)4} \rangle_{\boldsymbol{x}_s} / \langle \check{\omega}_1^{(s)2} \rangle_{\boldsymbol{x}_s}^2$. In this notation, the absence of the superindex d implies that the wavelet coefficients are directionally averaged. Specifically, Figs. 3(a) and 3(b) show that the flatness coefficients become increasingly larger than the Gaussian value 3 as the wavenumber increases. Also shown in the insets in Figs. 3(a) and 3(b) are the scale-conditioned flatness factors of the local spectra of kinetic energy

$$F_{\check{E}_k}(\kappa) = \langle \{\check{E}_k[\kappa, \boldsymbol{x}_s] - \check{E}_k(\kappa)\}^4 \rangle_{\boldsymbol{x}_s} / \langle \{\check{E}_k[\kappa, \boldsymbol{x}_s] - \check{E}_k(\kappa)\}^2 \rangle_{\boldsymbol{x}_s}^2 \tag{13}$$

and enstrophy

$$F_{\check{E}_\Omega}(\kappa) = \langle \{\check{E}_\Omega[\kappa, \boldsymbol{x}_s] - \check{E}_\Omega(\kappa)\}^4 \rangle_{\boldsymbol{x}_s} / \langle \{\check{E}_\Omega(\kappa, \boldsymbol{x}_s) - \check{E}_\Omega(\kappa)\}^2 \rangle_{\boldsymbol{x}_s}^2, \tag{14}$$

which display a similar trend of increasing intermittency as the wavenumber increases. These large variabilities in the spectra of the carrier phase have important consequences for the spectral characteristics of the particle concentration field, as shown below. It is worth mentioning that the
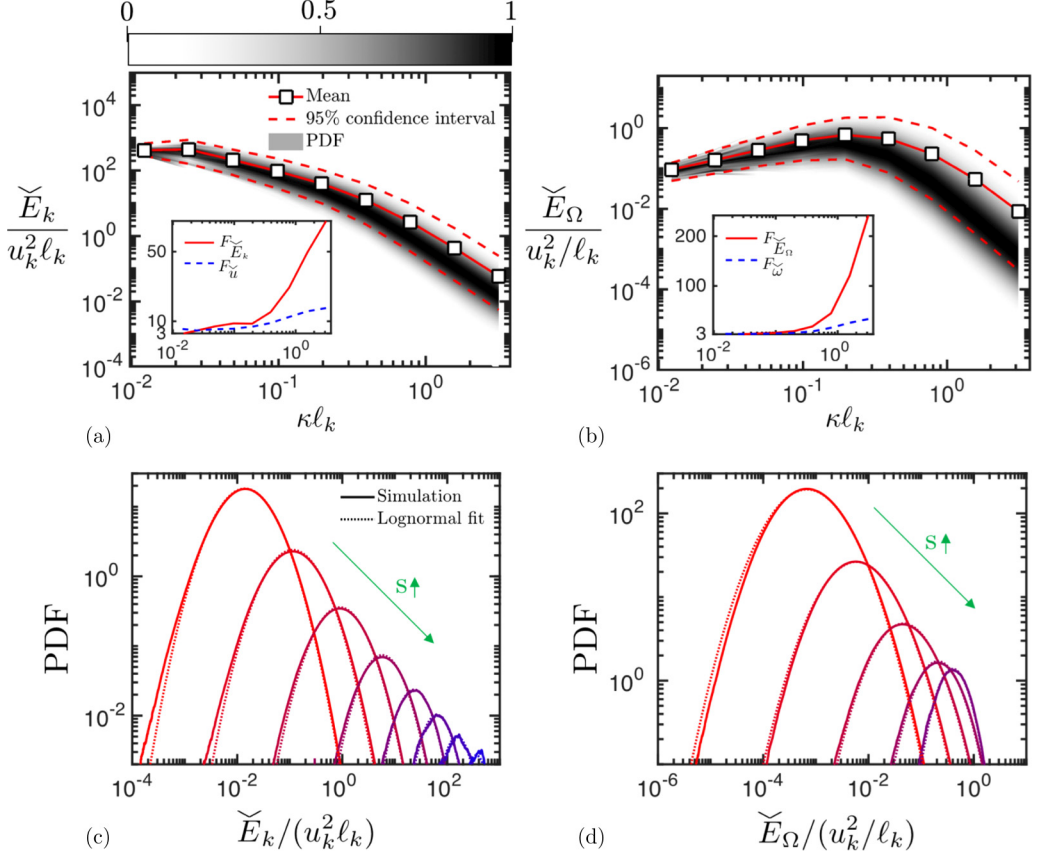
FIG. 3. Scale-dependent PDF of the wavelet spectra for (a) kinetic energy and (b) enstrophy, with solid lines indicating mean wavelet spectra, symbols denoting the discrete wavelet resolution levels $s = 1, 2, \ldots, 9$ ($\ell_s/\ell_k = 2^s$), and dashed lines corresponding to the 2.5th and 97.5th percentiles measuring the spatial variabilities of the spectra PDF. Insets in panels (a) and (b) show scale-conditioned spectral flatness factors of the energy spectra and wavelet coefficients of velocity and vorticity. Also shown in the figure are the scale-conditioned PDFs of (c) kinetic energy spectra (for scale indexes in the range $s = 1-8$) and (d) enstrophy spectra (for scale indexes in the range $s = 1-5$). Refer to panels (a) and (c) for legends of the panels (b) and (d), respectively.

flatness of the logarithm of the kinetic energy and enstrophy spectra approach values close to 3 at small scales [i.e., $F_{\ln \check{E}_k}(s = 1) = 3.01$ and $F_{\ln \check{E}_\Omega}(s = 1) = 2.9$], thereby confirming the nearly Gaussian structure of the variations of those logarithmically transformed quantities.

C. Dispersed-phase wavelet-based statistics

The scale-dependent analysis of the dispersed phase includes the analysis of the statistics of a coarse-grained particle number density $n_s[\boldsymbol{x}_s]$ and the wavelet spectra of the particle-number-density fluctuations, $\check{E}_\mathcal{N}$. The latter is related to the wavelet coefficients and is simply obtained by substituting $y = n$ in Eq. (11), while the former requires the introduction of approximation coefficients at intermediate scales, as described below.
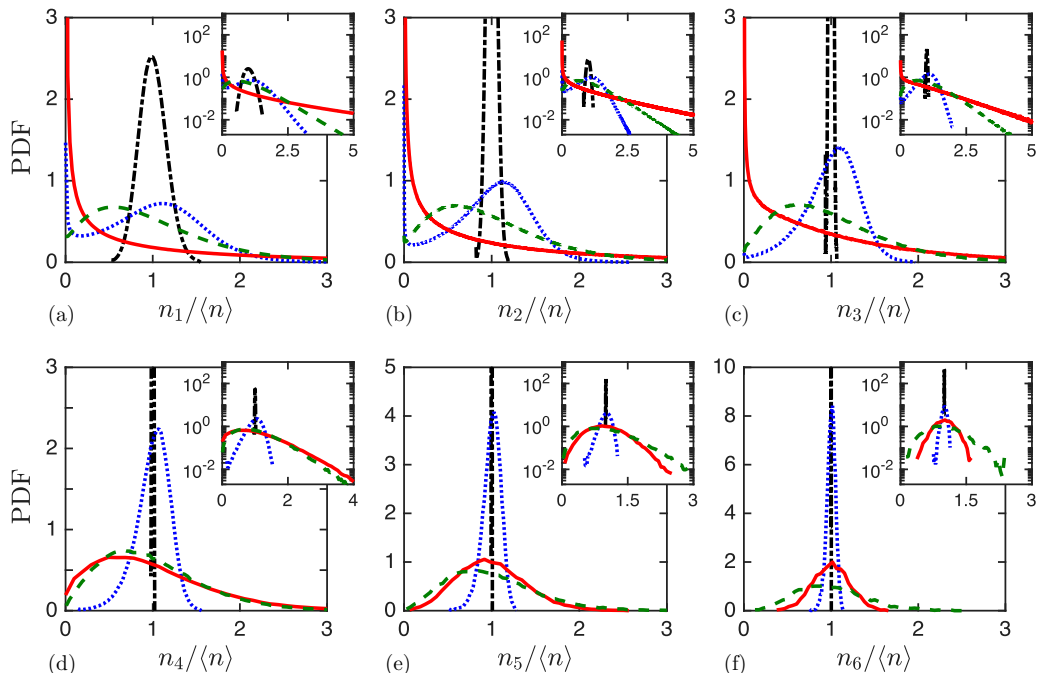
FIG. 4. Ensemble-averaged scale-dependent PDFs of the coarse-grained particle number density $n_s[\boldsymbol{x_s}]$ for (a) $\ell_1 = 2\ell_k$, (b) $\ell_2 = 4\ell_k$, (c) $\ell_3 = 8\ell_k$, (d) $\ell_4 = 16\ell_k$, (e) $\ell_5 = 32\ell_k$, and (f) $\ell_6 = 64\ell_k$. The lines correspond to $\mathrm{St}_k = 0.1$ (dotted blue line), $\mathrm{St}_k = 1$ (solid red line), $\mathrm{St}_k = 10$ (dashed green line), and random distribution (dash-dotted black line). Insets show the same data using a vertical logarithmic axis.

An alternative yet formally equivalent form of the wavelet-series expansion (6) in terms of the number density n is given by

$$n(\boldsymbol{x}) = \sum_{s=1}^{s'} \sum_{\boldsymbol{x_s}} \sum_{d=1}^{7} \check{n}^{(s,d)}[\boldsymbol{x_s}]\psi^{(s,d)}(\boldsymbol{x} - \boldsymbol{x_s}) + \sum_{\boldsymbol{x_{s'}}} \hat{n}^{(s')}[\boldsymbol{x_{s'}}]\phi^{(s')}(\boldsymbol{x} - \boldsymbol{x_{s'}}), \tag{15}$$

where

$$\hat{n}^{(s')}[\boldsymbol{x_{s'}}] = \langle n(\boldsymbol{x})\phi^{(s')}(\boldsymbol{x} - \boldsymbol{x_{s'}})\rangle \tag{16}$$

are approximation coefficients of y at an intermediate scale s' (i.e., $1 \leqslant s' \leqslant S$). Equation (16) can be obtained using the orthonormality properties of the wavelet and scaling functions $\psi^{(s,d)}(\boldsymbol{x} - \boldsymbol{x_s})$ and $\phi^{(s')}(\boldsymbol{x} - \boldsymbol{x_{s'}})$ [36]. The expansion (16) corresponds to stopping the MRA algorithm at an intermediate scale index s' instead of using it all the way up to the coarsest scale S.

In Eq. (15), the number density n is decomposed into a sum of fluctuations with characteristic length scales smaller than $\ell_{s'}$ (corresponding to the first term) and a broadband large-scale field that corresponds to a low-pass filtered n with cutoff length $\ell_{s'}$ (corresponding to the second term). The broadband large-scale field is defined in terms of approximation coefficients $\hat{n}^{(s')}[\boldsymbol{x_{s'}}]$ that represent a low-pass filtered version of n. Note that when Haar wavelets are used, the scaling functions $(N/2^{s'})^{3/2}\phi^{(s')}(\boldsymbol{x} - \boldsymbol{x_{s'}})$ are proportional to box filters with filter width $\ell_{s'}$. As a result, the coefficients $\hat{n}^{(s)}[\boldsymbol{x_s}]$ become proportional to a discrete, local coarse-grained particle number density $n_s[\boldsymbol{x_s}]$ that represents the mean value of n within the wavelet spatial support and is given by

$$n_s[\boldsymbol{x_s}] = \left(\frac{N}{2^s}\right)^{3/2} \hat{n}^{(s)}[\boldsymbol{x_s}], \tag{17}$$
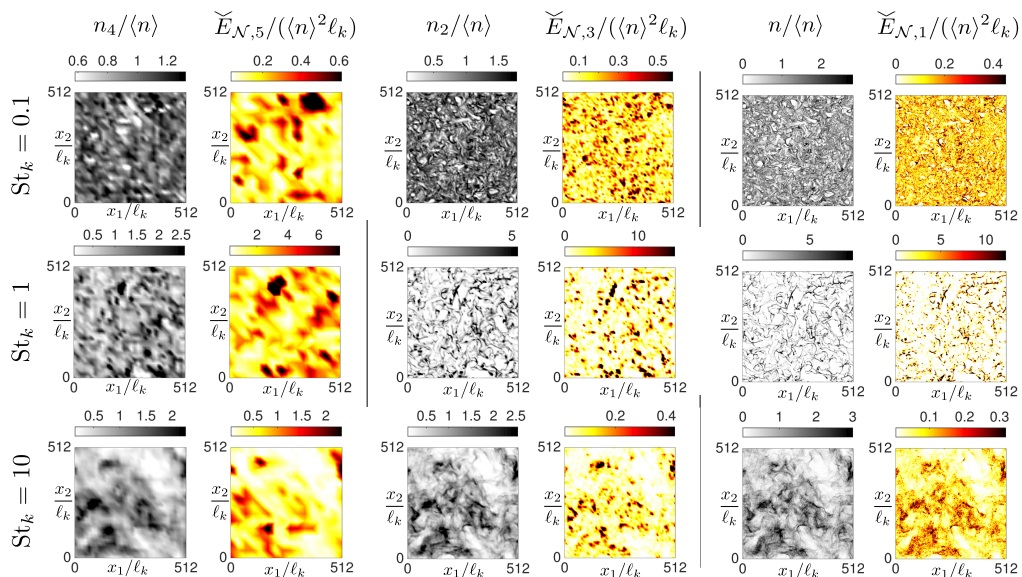
FIG. 5. Instantaneous mid-plane cross-sections of the particle number-density and associated local wavelet spectra at three length scales (columns) for three Stokes number (rows). The colormap axes range is chosen to represent the 95% confidence interval of the given quantity.

where the prime symbols have been omitted for convenience. In particular, the calculation of $n_s[\boldsymbol{x_s}]$ is equivalent to quantifying the number of particles in cubic boxes of side length ℓ_s centered at $\boldsymbol{x_s}$. The condition $\langle n_s[\boldsymbol{x_s}]\rangle_{\boldsymbol{x_s}} = \langle n \rangle$ is satisfied by construction, where the subindexed bracket operator denotes the discrete average over the wavelet collocation grid at the corresponding scale, namely $\langle n_s \rangle_{\boldsymbol{x_s}} = (2^s/N)^3 \sum_{\boldsymbol{x_s}} n_s$.

The PDFs of n_s normalized by the volume average $\langle n \rangle$ are shown in Fig. 4. A zero value for n_s indicates the presence of a void of size ℓ_s centered at $\boldsymbol{x_s}$, whereas a large value $n_s \gg \langle n \rangle$ denotes a spatial region of size ℓ_s centered at $\boldsymbol{x_s}$ representative of clustering. At small scales, the PDF of n_s for $\mathrm{St}_k = 1$ differs significantly from those corresponding to $\mathrm{St}_k = 0.1$ and $\mathrm{St}_k = 10$. The former has a higher content of extreme values representing many voids and intensely concentrated clusters. In contrast, the PDFs of n_s for $\mathrm{St}_k = 0.1$ and $\mathrm{St}_k = 10$ have a shape relatively more similar to the Poisson PDF. As ℓ_s increases, both voids and clusters disappear in all PDFs. For instance, for $s > 4$ the voids have disappeared in the cases $\mathrm{St}_k = 0.1$ and 10, but they persist until $s = 5$ for $\mathrm{St}_k = 1$. As the scale is further increased, all PDFs increasingly resemble a Dirac delta function centered at $\langle n \rangle$. As shown in Fig. 4(f), this similarity is more pronounced for the case $\mathrm{St}_k = 0.1$, which does not display any significant preferential concentration phenomenon at large scales and is followed by the cases $\mathrm{St}_k = 1$ and $\mathrm{St}_k = 10$, the latter containing preferential concentration of particles at the large scales, as suggested by the broad patches of particles visualized in the third row of the first column in Fig. 1.

In addition to the considerations given above, Fig. 4 also illustrates the scale dependency of the preferential concentration effect. Particles at $\mathrm{St}_k = 1$ tend to preferentially concentrate at small scales, and therefore the range and shape of the PDF of n_s for that case in Fig. 4, along with the corresponding spatial contours of n_s in Fig. 5, vary largely as the scale is increased. On the other hand, particles at $\mathrm{St}_k = 10$ do not preferentially concentrate significantly at small scales, but they do so at large scales since $\mathrm{St}_\ell \sim \mathrm{St}_k/\mathrm{Re}_\ell^{1/2} \sim 0.5$, thereby forming broad clouds of particles. This leads to relatively more resilient contours and shapes of the PDF of n_s as the scale is increased.

In interpreting these results, it is worth returning briefly to the results shown in Fig. 2(d) for the Fourier spectrum of the full concentration field n and noticing that the spectral energies become
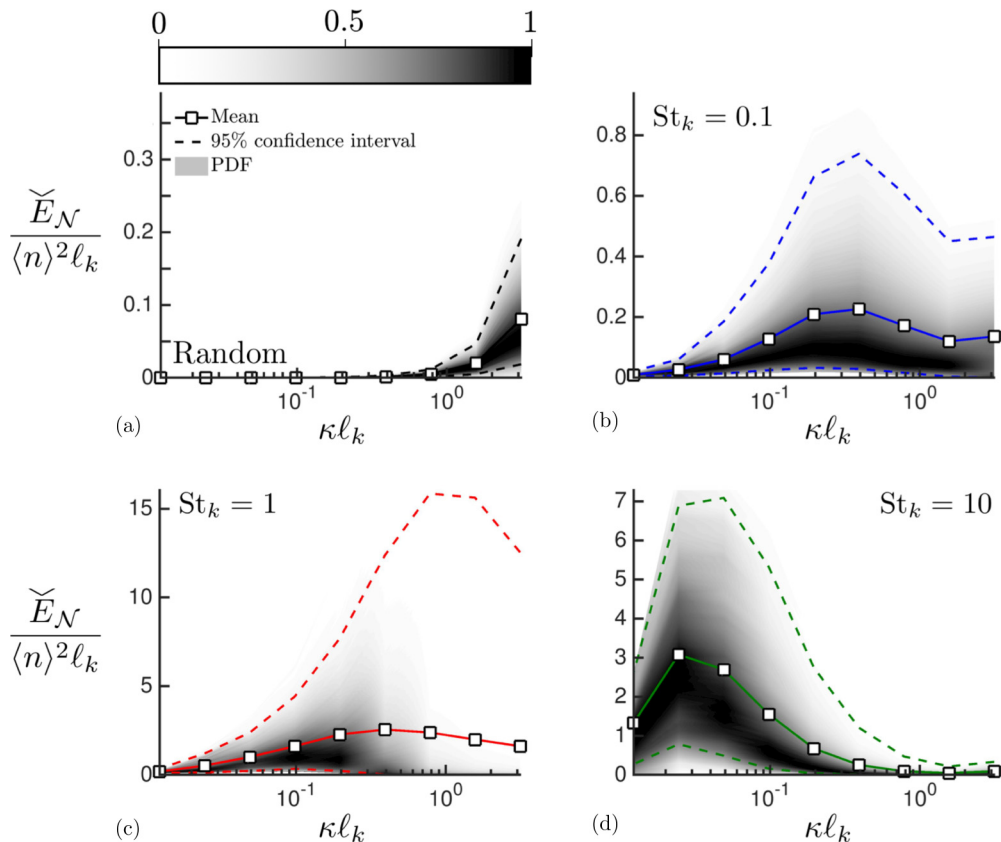
FIG. 6. Contours of the ensemble-averaged wavelet spectra of particle concentration energy for (a) random distribution, (b) $St_k = 0.1$, (c) $St_k = 1.0$, and (d) $St_k = 10$, with solid lines indicating mean wavelet spectra, symbols denoting the discrete wavelet resolution levels $s = 1, 2, \ldots, 9$ ($\ell_s/\ell_k = 2^s$), and dashed lines corresponding to the 2.5th and 97.5th percentiles measuring the spatial variabilities of the spectra PDF.

maximum at the large scales (for $St_k = 10$) and at small scales (for $St_k = 0.1$ and 1), where the enstrophy spectrum peaks (see also Ref. [21] for similar results). The magnitude of the peak in spectral energy becomes largest for $St_k = 10$, followed by $St_k = 1$ and $St_k = 0.1$. However, note that the total energy of the fluctuations of the concentration field (or equivalently its variance) is the largest for $St_k = 1$ among the three cases and is mostly concentrated in the high-wavenumber portion of the spectrum. This implies, for instance, that the broad clouds observed for $St_k = 10$ are necessarily less intensely concentrated than the thin clusters obtained for $St_k = 1$, as observed in Fig. 4(f) by the resulting narrower PDF of n_s for $St_k = 10$ in comparison with the broader PDF for $St_k = 1$ at small scales in Fig. 4(a).

The aforementioned Fourier spectra, however, do not account for the spatial localization of the number-density structures observed in regimes where preferential concentration is important. This limitation can be circumvented by examining the wavelet-based spectra $\check{E}_\mathcal{N}$ of the concentration fluctuations, as shown in Figs. 5 and 6. Note that the value of the energy spectrum $\check{E}_\mathcal{N}$ at scale s is related to the fluctuations of the coarse-grained particle number density field $n_{s-1}[\boldsymbol{x_{s-1}}]$ at scale $s-1$ in the following way. As indicated in Eq. (11), $\check{E}_\mathcal{N}$ is computed based on the wavelet coefficients $\check{n}^{(s,d)}[\boldsymbol{x_s}]$ at the same scale. However, in the MRA algorithm, the wavelet coefficients $\check{n}^{(s,d)}[\boldsymbol{x_s}]$ are computed recursively based on the approximation coefficients $\hat{n}^{(s-1)}[\boldsymbol{x_{s-1}}]$ at the previous scale (see Ref. [36] for more details on the algorithm). Physically, the determination of a fluctuation of n and its
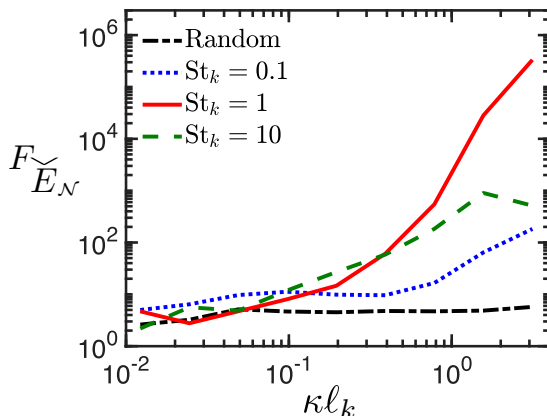
FIG. 7. Scale-dependent flatness factor of wavelet spectra.

energy at scale s requires information of the spatial variations of the coarse-grained number density field n_{s-1} at the previous scale.

Based on the above considerations, Fig. 5 provides $\check{E}_{\mathcal{N}}$ at three scales with the corresponding coarse-grained field n_{s-1} side by side. The wavelet spectrum $\check{E}_{\mathcal{N}}$ becomes locally zero in regions void of particles since $\check{n}^{(s,d)} = 0$ there. In contrast, $\check{E}_{\mathcal{N}}$ is large in regions where the fluctuations of n are large, such as those encountered around and within particle clusters, since $\check{n}^{(s,d)}$ is maximum there. A recent study [32] has exploited these properties of wavelets for discerning structures of the particle concentration field, and for subsequently formulating algorithms for automatic adaption of grids around particle clusters using wavelet filters.

The contours of the PDFs of the wavelet spectra are shown in Fig. 6, which includes spatial averages and spatial variabilities. Note that the spatial averages of the spectra resemble those shown in Fig. 2 based on Fourier analyses, as highlighted in earlier work focused on single-phase turbulence [26,31]. Below a Stokes-number-dependent characteristic scale, the 2.5th percentile of the PDF is zero, corresponding to regions void of particles. In contrast, the spectra reach large values well above the spatial mean in regions where the particles accumulate. For instance, at $St_k = 1$, it is observed that at the scale corresponding to the maximum of the spatial mean, the local values of the spectra can be one order of magnitude larger than the mean. These disparities are not observed in the case of randomly distributed particles, and they are also largely attenuated for $St_k = 0.1$ and $St_k = 10$. The large variations of the concentration spectra mentioned above, particularly for $St_k = 1$, are quantified in Fig. 7 by the spectral flatness factor

$$F_{\check{E}_{\mathcal{N}}}(\kappa) = \langle \{\check{E}_{\mathcal{N}}[\kappa, \boldsymbol{x}_s] - \check{E}_{\mathcal{N}}(\kappa)\}^4 \rangle_{\boldsymbol{x}_s} / \langle \{\check{E}_{\mathcal{N}}[\kappa, \boldsymbol{x}_s] - \check{E}_{\mathcal{N}}(\kappa)\}^2 \rangle_{\boldsymbol{x}_s}^2. \tag{18}$$

As the scale decreases, the results indicate that $F_{\check{E}_{\mathcal{N}}}$ deviates from the spectral flatness of the spectra of the randomly distributed particles, most rapidly for $St_k = 1$, where the intermittency of the concentration field is the largest. At $St_k = 1$, the PDF of $\check{E}_{\mathcal{N}}$ transitions from log-normal-like (at large scales), where no voids are observed, to an exponential-like distribution (at small scales), where voids are observed. The transition occurs at $s = 4$ corresponding to the length scale $\ell_4 = 16\ell_k$, which represents the largest size of the voids observed in the simulations. Note, however, that these results are contingent on the density-estimation method utilized here (see Sec. II) and that other different methods such as Voronoi tessellation may render small but nonzero number-density values even in the core of strong vortices [3].

The results described above are in accord with early work on the scale dependency of preferential concentration that made use of methods different from wavelets. These include, for instance, studies highlighting the dependence of a global preferential-concentration index on the grid resolution used

for estimating the coarse-grained particle number density and on the Stokes number [2,40], which suggested that (a) the grid resolution that maximizes the global preferential-concentration index increases with Stokes number and (b) for Stokes numbers less than or equal to 1, the scales at which the global preferential-concentration index peak are of order 10 to 20 Kolmogorov lengths, corresponding to wavelet scale indexes $s \sim 3$–4 in the present study.

D. Interphase wavelet-based statistics

In Sec. III B, the analysis highlighted the spatial variability associated with the local turbulence dynamics, as illustrated, for instance, by the sparsity observed in the log-normal-like PDFs of the carrier-phase spectra in Fig. 3, with few wavelet modes capturing most of the energy [29]. In Sec. III C, the preferential concentration of particles is observed to lead to highly inhomogeneous particle number-density fields, as illustrated, for instance, by the PDFs of n_s in Fig. 4 and by the energy spectra of n in Fig. 6, which strongly differ from those obtained when the particles are randomly distributed. The spatial localization properties of the wavelet basis also enables the cross-correlated analysis of spectral characteristics between the two different phases. A number of different metrics may be formulated to this end, but perhaps the simplest ones relate to conditional statistics and joint PDFs, as described below.

A question that can be naturally addressed using wavelets is the characteristics of the carrier-phase spectrum in zones where the particle density is large or small. For this purpose, it is expedient to correlate the carrier-phase spectra with the number density field. For consistency with the spatial support of the spectra at each scale, the correlations are performed by employing the scale-dependent coarse-grained number density n_s defined in Sec. III C.

Based on these considerations, Figs. 8 and 9 show the spatial mean of n_s (with $s = 1$–4) conditioned on the fluctuations of the logarithm of the local wavelet spectra of kinetic energy and enstrophy, $(\ln \check{E}_k)' = \ln \check{E}_k - \langle \ln \check{E}_k \rangle_{\boldsymbol{x}_s}$ and $(\ln \check{E}_\Omega)' = \ln \check{E}_\Omega - \langle \ln \check{E}_\Omega \rangle_{\boldsymbol{x}_s}$, normalized with the corresponding standard deviations $\sigma_{\ln \check{E}_k}$ and $\sigma_{\ln \check{E}_\Omega}$. For given values of St_k and s, this leads to curves centered at zero value in the abscissa with a mostly similar and symmetric range resulting from the near Gaussianity of the logarithm of the wavelet spectra of the carrier phase, in a way that allows comparisons with curves subject to different values of those two parameters. Physically, the conditional means provide a measure of how much clustered the particles are depending on the fluctuations of the spectra with respect to $\langle \ln \check{E}_k \rangle_{\boldsymbol{x}_s}$ and $\langle \ln \check{E}_\Omega \rangle_{\boldsymbol{x}_s}$. Note, however, that, because of the logarithmic transformation, these two mean values are shifted below the logarithm of the mean values of the spectra [represented by the solid lines in Figs. 3(a) and 3(b)] by $\sigma^2_{\ln \check{E}_k}/2$ and $\sigma^2_{\ln \check{E}_\Omega}/2$, respectively. It is worth emphasizing that the resulting trends remain similar to those observed when the conditioning is made with respect to $\check{E}_k$ and $\check{E}_\Omega$ instead, but the curves are considerably less visually convenient because of the wide range of values attained by the spectra.

The results in Figs. 8 and 9 indicate that anticorrelations develop between the energy spectra and n_s at small scales in regimes where preferential concentration is important, thereby suggesting that particles preferentially sample flow regions where the enstrophy and kinetic-energy spectra are much smaller than their corresponding spatial averages. For instance, for $\mathrm{St}_k = 1$ and at the smallest scale $s = 1$, the conditional mean indicates that two times fewer particles are found on average in regions where the spectrum is largest, with up to two times more being found on average in quieter regions of the flow. Note that such anticorrelation vanishes rapidly away from preferentially concentrated regimes $\mathrm{St}_k = 1$, with particles showing much less preference for the local spectral dynamics of the carrier phase in the cases $\mathrm{St}_k = 0.1$ and $\mathrm{St}_k = 10$, which resemble more the uncorrelation found in the case where the particles are randomly located in the flow. In particular, the particles in the case $\mathrm{St}_k = 0.1$ tend to avoid regions of space with high positive fluctuations of the spectra more prominently that the particles in the case $\mathrm{St}_k = 10$, and tend to sample flow regions where the spectra is close to or smaller than the spatial mean. Similarly, the anticorrelation vanishes as the length scale is increased in both spectra in accordance with the decreasingly smaller values of the associated flatness coefficients.
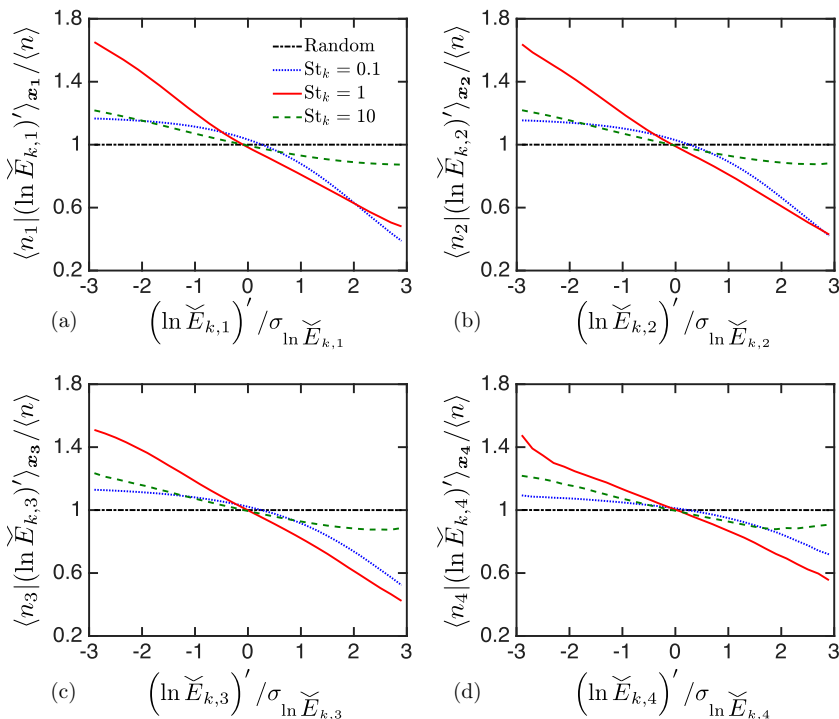
FIG. 8. Spatial mean of the coarse-grained particle-number density conditioned on the fluctuation of the logarithm of the carrier-phase kinetic-energy spectrum for (a) $\ell_1 = 2\ell_k$, (b) $\ell_2 = 4\ell_k$, (c) $\ell_3 = 8\ell_k$, and (d) $\ell_4 = 16\ell_k$.

A compact representation of the aforementioned results is shown in Fig. 10 in the form of contours of the joint PDF between the fluctuations of the logarithm of the spectra and the scale-dependent coarse-grained number density. The results there are particularized at scale index $s = 4$ (i.e., $\ell_4 = 16\ell_k$) where the mean number-density spectrum in the case $\mathrm{St}_k = 1$ reaches maximum values. The stretching and tilting generated in the joint PDF between the enstrophy spectrum and the number density by the preferential concentration effect become evident for the case $\mathrm{St}_k = 1$ in comparison with the mostly circularly symmetric joint PDF observed in the case of randomly distributed particles.

IV. CONCLUSIONS

In this study, DNS of incompressible homogeneous-isotropic turbulence laden with a dilute suspension of point particles are performed in conjunction with a wavelet multiresolution analysis of the results aimed at investigating the local spectral characteristics of the preferential concentration of small inertial particles in turbulence. The spatial localization of the wavelet-basis functions facilitate the simultaneous study of physical and scale spaces in the spectral characterization of the flow field of the carrier phase and the concentration field of the dispersed phase.

The wavelet analysis of the dispersed phase provides statistical information about the spatial variabilities of the scale-dependent coarse-grained number density field n_s and the energy spectra of its fluctuations. In the preferentially concentrated regime $\mathrm{St}_k = 1$, the PDF of n_s varies rapidly as the scale is varied, while cases where the particles are ballistic do not show such high sensitivity to scale. Similarly, a limiting length scale of order $32\ell_k$, which is representative of the wavenumber where the spatially averaged enstrophy spectrum is maximum, is observed at $\mathrm{St}_k = 1$ above which no voids are discerned in the particle-concentration field. Also at $\mathrm{St}_k = 1$ the spatial variabilities of the wavelet energy spectrum of the particle concentration fluctuations are observed to be maximum.
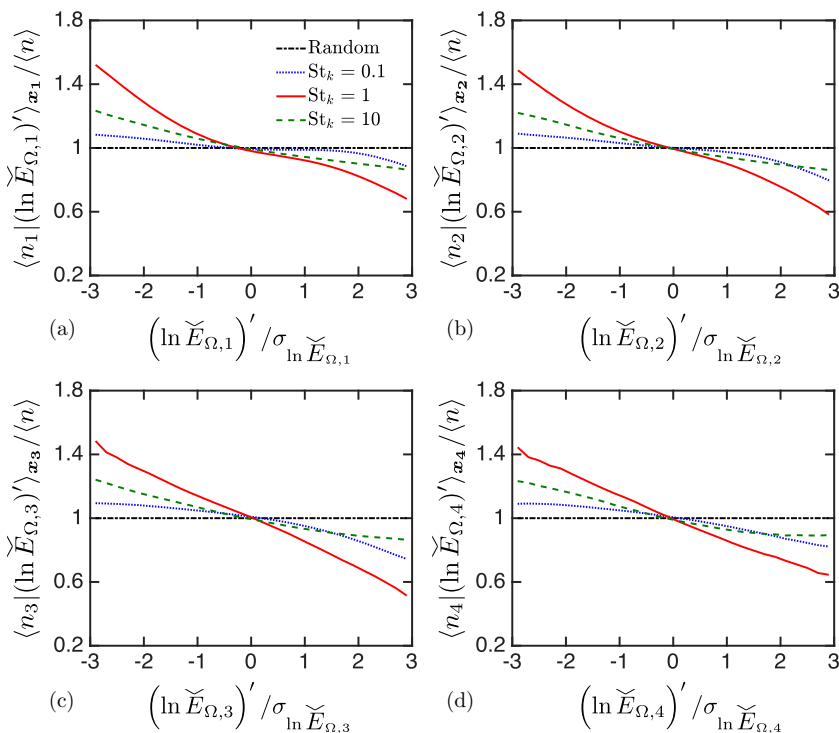
FIG. 9. Spatial mean of the coarse-grained particle-number density conditioned on the fluctuation of the logarithm of the carrier-phase enstrophy spectrum for (a) $\ell_1 = 2\ell_k$, (b) $\ell_2 = 4\ell_k$, (c) $\ell_3 = 8\ell_k$, and (d) $\ell_4 = 16\ell_k$.
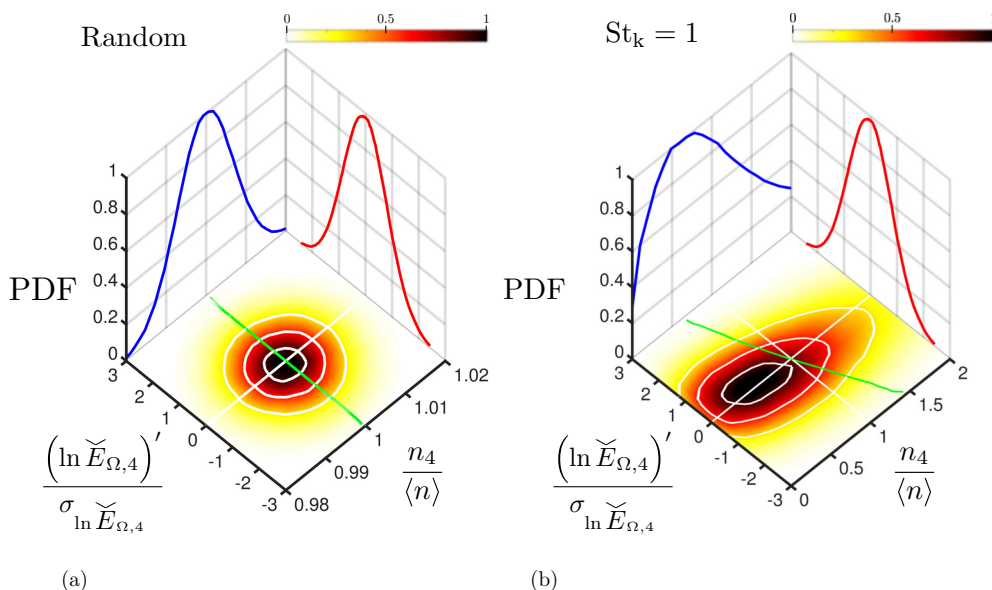

FIG. 10. Marginal PDFs (blue and red lines), joint PDFs (solid contours and white isolines normalized with the PDF maximum), and conditional means (green lines) of the scale-dependent coarse-grained particle number density and carrier-phase enstrophy spectrum at $s = 4$ (i.e., $\ell_s = 16\ell_k$) for (a) randomly distributed particles and (b) $St_k = 1$ particles.

An interphase wavelet-based analysis is performed that reports cross correlations between the particle-concentration field and the local spectrum of the carrier phase. In preferentially concentrated regimes, a spatial anticorrelation is found between those quantities by which the particles preferentially sample flow regions where the enstrophy and kinetic-energy spectra are much smaller than their corresponding spatial averages. The anticorrelation vanishes as the length scale of the wavelet collocation grid is increased and is largely suppressed in regimes where preferential concentration is not important.

To the best of the authors' knowledge, the present study is one of the first reporting spatial cross correlations between carrier-phase energy spectra and dispersed-phase field variables in turbulence laden with inertial particles. Application of the present results to subgrid-scale (SGS) modeling for large-eddy simulations (LES) of particle-laden turbulence [22,41–50] represents a worthwhile topic for future work. In particular, in SGS models of kinematic-simulation type [48–50], the regeneration of the missing scales of turbulence is made by incorporating high-wavenumber Fourier modes in the velocity field using spectral extrapolation. In order to impose that the energy spectrum of the SGS velocity matches a prescribed one obtained either from DNS or theory, the SGS flow field is typically obtained by randomly sampling wavevectors in spectral space [50]. However, this procedure limits the generation of small-scale coherent structures responsible for particle clustering, since the second-order statistics alone do not contain information about the localization of the turbulent structures, the latter being lost in the phase of all coefficients in Fourier space. The present study suggests that in SGS modeling for particle-laden turbulence based on spectral enrichment, matching the second-order statistics of the velocity field is desirable but probably not sufficient. This is because the spatial distribution of spectral energy, computed here using localized wavelet spectra, is closely related to the spatial distribution of particles. As a consequence, spatial PDFs quantifying variabilities of SGS turbulence spectral dynamics may represent relevant metrics to be matched by predictive SGS models for particle-laden turbulence. To this end, wavelet-based models would appear to be more advantageous than Fourier-based models because they could encode local spectral information.

ACKNOWLEDGMENT

---

[1] B. J. Lazaro and J. C. Lasheras, Particle dispersion in a turbulent, plane, free shear layer, Phys. Fluids A 1, 1035 (1989).

[2] A. Aliseda, A. Cartellier, F. Hainaux, and J. C. Lasheras, Effect of preferential concentration on the settling velocity of heavy particles in homogeneous isotropic turbulence, J. Fluid Mech. 468, 77 (2002).

[3] R. Monchaux, M. Bourgoin, and A. Cartellier, Preferential concentration of heavy particles: A Voronoï analysis, Phys. Fluids 22, 103304 (2010).

[4] J. P. Minier, On Lagrangian stochastic methods for turbulent polydisperse two-phase reactive flows, Prog. Energy Combust. Sci. 50, 1 (2015).

[5] M. Rahmani, G. Geraci, G. Iaccarino, and A. Mani, Effects of particle polydispersity on radiative heat transfer in particle-laden turbulent flows, Int. J. Multiphase Flow 104, 42 (2018).

[6] M. Di Renzo and J. Urzay, Aerodynamic generation of electric fields in turbulence laden with charged inertial particles, Nat. Commun. 9, 1676 (2018).

[7] L. Jofre, G. Geraci, H. Fairbanks, A. Doostan, and G. Iaccarino, Multi-fidelity uncertainty quantification of irradiated particle-laden turbulence, Annual Research Briefs, Center for Turbulence Research (Stanford University, 2017), pp. 21–34.

[8] A. Ferrante and S. Elghobashi, On the physical mechanisms of two-way coupling in particle-laden isotropic turbulence, Phys. Fluids **15**, 315 (2003).

[9] A. Frankel, H. Pouransari, F. Coletti, and A. Mani, Settling of heated particles in homogeneous turbulence, J. Fluid Mech. **792**, 869 (2016).

[10] D. H. Richter, O. Garcia, and C. Astephen, Particle stresses in dilute, polydisperse, two-way coupled turbulent flows, Phys. Rev. E **93**, 013111 (2016).

[11] H. Pouransari and A. Mani, Effects of preferential concentration on heat transfer in particle-based solar receivers, J. Sol. Energy Eng. **139**, 021008 (2017).

[12] M. Esmaily and A. Mani, Analysis of the clustering of inertial particles in turbulent flows, Phys. Rev. Fluids **1**, 084202 (2016).

[13] L. Villafañe, A. Banko, C. Elkins, and J. K. Eaton, Gas heating by radiation absorbing inertial particles in a turbulent duct flow, Annual Research Briefs, Center for Turbulence Research (Stanford University, 2017), pp. 35–47.

[14] J. A. K. Horwitz and A. Mani, Correction scheme for point-particle models applied to a nonlinear drag law in simulations of particle-fluid interaction, Int. J. Multiphase Flow **101**, 74 (2018).

[15] A. Robinson, On the motion of small particles in a potential field of flow, Commun. Pure Appl. Math. **9**, 69 (1956).

[16] J. F. De La Mora and P. Riesco-Chueca, Aerodynamic focusing of particles in a carrier gas, J. Fluid Mech. **195**, 1 (1988).

[17] D. Martinez-Ruiz, J. Urzay, A. L. Sánchez, A. Liñán, and F. A. Williams, Dynamics of thermal ignition of spray flames in mixing layers, J. Fluid Mech. **734**, 387 (2013).

[18] A. L. Sánchez, J. Urzay, and A. Liñán, The role of separation of scales in the description of spray combustion, Proc. Combust. Inst. **35**, 1549 (2015).

[19] M. R. Maxey, The gravitational settling of aerosol particles in homogeneous turbulence and random flow fields, J. Fluid Mech. **174**, 441 (1987).

[20] K. D. Squires and J. K. Eaton, Preferential concentration of particles by turbulence, Phys. Fluids **3**, 1169 (1991).

[21] G. Jin, G. H. He, and L. P. Wang, Large-eddy simulation of turbulent collision of heavy particles in isotropic turbulence, Phys. Fluids **22**, 055106 (2010).

[22] G. I. Park, M. Bassenne, J. Urzay, and P. Moin, A simple dynamic subgrid-scale model for LES of particle-laden turbulence, Phys. Rev. Fluids **2**, 044301 (2017).

[23] G. K. Batchelor and A. A. Townsend, The nature of turbulent motion at large wave-numbers, Proc. R. Soc. London, Ser. A **199**, 238 (1949).

[24] E. K. Longmire and J. K. Eaton, Structure of a particle-laden round jet, J. Fluid Mech. **236**, 217 (1992).

[25] L. P. Wang and M. R. Maxey, Settling velocity and concentration distribution of heavy particles in homogeneous isotropic turbulence, J. Fluid Mech. **256**, 27 (1993).

[26] C. Meneveau, Analysis of turbulence in the orthonormal wavelet representation, J. Fluid Mech. **232**, 469 (1991).

[27] K. Yoshimatsu, N. Okamoto, K. Schneider, Y. Kaneda, and M. Farge, Intermittency and scale-dependent statistics in fully developed turbulence, Phys. Rev. E **79**, 026303 (2009).

[28] J. P. Ruppert-Felsot, M. Farge, and P. Petitjeans, Wavelet tools to study intermittency: Application to vortex bursting, J. Fluid Mech. **636**, 427 (2009).

[29] K. Schneider and O. Vasilyev, Wavelet methods in computational fluid dynamics, Annu. Rev. Fluid Mech. **42**, 473 (2010).

[30] J. Urzay, A. Doostmohammadi, and J. M. Yeomans, Multi-scale statistics of turbulence motorized by active matter, J. Fluid Mech. **822**, 762 (2017).

[31] M. Farge, Wavelet transforms and their applications to turbulence, Annu. Rev. Fluid Mech. **24**, 395 (1992).

[32] M. Bassenne, J. Urzay, K. Schneider, and P. Moin, Extraction of coherent clusters and grid adaptation in particle-laden turbulence using wavelet filters, Phys. Rev. Fluids **2**, 054301 (2017).

[33] M. Bassenne, J. Urzay, G. I. Park, and P. Moin, Constant-energetics physical-space forcing methods for improved convergence to homogeneous-isotropic turbulence with application to particle-laden flows, Phys. Fluids **28**, 035114 (2016).

[34] H. Pouransari, M. Mortazavi, and A. Mani, Parallel variable-density particle-laden turbulence simulation. Annual Research Briefs, Center for Turbulence Research (Stanford University, 2015), pp. 43–54.

[35] P. S. Addison, *The Illustrated Wavelet Transform Handbook: Introductory Theory and Applications in Science, Engineering, Medicine, and Finance* (CRC Press, Boca Raton, FL, 2017).

[36] S. G. Mallat, A theory for multiresolution signal decomposition: The wavelet representation, IEEE T. Pattern Anal. **11**, 674 (1989).

[37] R. Nguyen van Yen, D. del-Castillo-Negrete, K. Schneider, M. Farge, and G. Chen, Wavelet-based density estimation for noise reduction in plasma simulations using particles, J. Comput. Phys. **229**, 2821 (2010).

[38] G. Kutyniok and D. Labate, *Shearlets: Multiscale Analysis for Multivariate Data*, Applied and Numerical Harmonic Analysis (Birkhauser, Boston, 2012), pp. 1–38.

[39] V. Perrier, T. Philipovitch, and C. Basdevant, Wavelet spectra compared to Fourier spectra, J. Math. Phys. **36**, 1506 (1995).

[40] R. Monchaux, M. Bourgoin, and A. Cartellier, Analyzing preferential concentration and clustering of inertial particles in turbulence, Int. J. Multiphase Flow **40**, 1 (2012).

[41] J. Pozorski and S. V. Apte, Filtered particle tracking in isotropic turbulence and stochastic modeling of subgrid-scale dispersion, Int. J. Multiphase Flow **35**, 118 (2009).

[42] G. Jin and G. He, A nonlinear model for the subgrid timescale experienced by heavy particles in large eddy simulation of isotropic turbulence with a stochastic differential equation, New J. Phys. **15**, 035011 (2013).

[43] J. Urzay, M. Bassenne, G. I. Park, and P. Moin, Characteristic regimes of subgrid-scale coupling in LES of particle-laden turbulent flows, Annual Research Briefs, Center for Turbulence Research (Stanford University, 2014), pp. 3–13.

[44] C. Marchioli, Large-eddy simulation of turbulent dispersed flows: A review of modelling approaches, Acta Mech. **228**, 741 (2017).

[45] M. Gorokhovski and R. Zamansky, Modeling the effects of small turbulent scales on the drag force for particles below and above the Kolmogorov scale, Phys. Rev. Fluids **3**, 034602 (2018).

[46] M. Bassenne, M. Esmaily, D. Livescu, P. Moin, and J. Urzay, Dynamic spectrally enriched LES subgrid-scale modeling for preferential concentration of inertial particles in turbulence, Annual Research Briefs, Center for Turbulence Research (Stanford University, 2017), pp. 3–19.

[47] J. G. M. Kuerten and A. W. Vreman, Can turbophoresis be predicted by large-eddy simulation? Phys. Fluids **17**, 011701 (2005).

[48] C. Gobert and M. Manhart, Subgrid modelling for particle-LES by spectrally optimized interpolation (SOI), J. Comput. Phys. **230**, 7796 (2011).

[49] S. Murray, M. F. Lightstone, and S. Tullis, Single-particle lagrangian and structure statistics in kinematically simulated particle-laden turbulent flows, Phys. Fluids **28**, 033302 (2016).

[50] B. Ray and L. R. Collins, A subgrid model for clustering of high-inertia particles in large-eddy simulations of turbulence, J. Turbul. **15**, 366 (2014).